NANOMATERIALS

Chemical scissor-mediated structural editing of layered transition metal carbides

Haoming Ding^{1,2,3}, Youbing Li^{1,3}, Mian Li^{1,3}, Ke Chen^{1,3}, Kun Liang^{1,3}, Guoxin Chen³, Jun Lu⁴, Justinas Palisaitis⁴, Per O. Å. Persson⁴, Per Eklund⁴, Lars Hultman⁴, Shiyu Du^{1,2,3}, Zhifang Chai^{1,2,3}, Yury Gogotsi⁵*, Qing Huang^{1,3,6}*

Intercalated layered materials offer distinctive properties and serve as precursors for important two-dimensional (2D) materials. However, intercalation of non-van der Waals structures, which can expand the family of 2D materials, is difficult. We report a structural editing protocol for layered carbides (MAX phases) and their 2D derivatives (MXenes). Gap-opening and species-intercalating stages were respectively mediated by chemical scissors and intercalants, which created a large family of MAX phases with unconventional elements and structures, as well as MXenes with versatile terminals. The removal of terminals in MXenes with metal scissors and then the stitching of 2D carbide nanosheets with atom intercalation leads to the reconstruction of MAX phases and a family of metal-intercalated 2D carbides, both of which may drive advances in fields ranging from energy to printed electronics.

ntercalated materials are predominantly produced by introducing non-native species into the van der Waals (vdW) gaps of inherently layered vdW materials such as graphite, hexagonal boron nitride, and transition metal dichalcogenides (1, 2). Guesthost interactions alter the electronic structure and enable property tailoring for energy storage, catalysis, electronic, optical, and magnetic applications (3–7). $M_{n+1}AX_n$, or "MAX phases," are a large family of ternary layered compounds that typically have weak metallic bonds between M and A atoms and covalent bonds within the $M_{n+1}X_n$ layers (8, 9). Here, M denotes an early transition element. A is a main group element, X is nitrogen and/or carbon, and n is a number between one and four. The strong non-vdW bonding in MAX phases requires chemical etching of A elements to obtain their two-dimensional (2D) derivatives, MXenes (10-12). The resultant vdW gaps in MXenes provide space for intercalating various guest species. For example, anions such as F⁻, O²⁻, OH⁻, and Cl⁻ spontaneously coordinate with exposed M atoms of MXenes as termination species T, as described by the $M_{n+1}X_nT_x$ formula (10, 13). Intercalation of cations, cationic surfactants, and organic molecules in vdW gaps expands the interlayer spacing of MXenes and facilitates their

¹Engineering Laboratory of Advanced Energy Materials, Ningbo Institute of Materials Technology and Engineering, Chinese Academy of Sciences, Ningbo, Zhejiang 315201, China. ²University of Chinese Academy of Sciences, 19 A Yuquan Rd, Shijingshan District, Beijing 100049, China. ³Qianwan Institute of CNITECH, Ningbo, Zhejiang 315336, China. ⁴Thin Film Physics Division, Department of Physics, Chemistry, and Biology (IFM), Linköping University, SE-581 83 Linköping, Sweden. ⁵Department of Materials Science and Engineering, A. J. Drexel Nanomaterials Institute, Drexel University, Philadelphia, PA 19104, USA. ⁶Advanced Energy Science and Technology Guangdong Laboratory, Huizhou, Guangdong 516003, China.

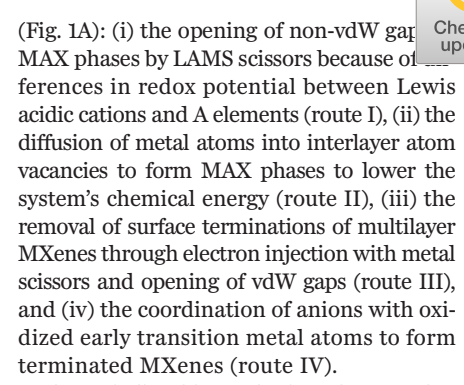
*Corresponding authors. Email: huangqing@nimte.ac.cn (Q.H.); gogotsi@drexel.edu (Y.G.)

delamination into monolayers, finding roles in energy storage, printed electronics, electromagnetic interference shielding, and many other applications (14–16).

Recently, we reported a Lewis acidic molten salt (LAMS) etching protocol that is capable of both etching and substituting weakly bonded interlayer atoms in MAX phases (13). A series of MAX phases containing late transition metals and MXenes with pure halogen terminations were synthesized and explored for applications as catalysts and ferromagnetic and electrochemical energy storage materials (17-20). However, only a few LAMSs have thermophysical (solubility, melting point, and boiling point) and chemical (redox potential and activity of cations and coordination geometry of anions) properties required to act as both etchant and intercalant. For example, MXenes with -O, -S, -Se, -Te, and -NH terminations were only realized by an anion exchange reaction with brominated MXenes (21). The direct use of oxides or chalcogenides with strong covalent bonds to supply -O and chalcogen terminations would be a daunting task because of their high melting temperature and low solubility, both of which substantially limit the structural editing capability of LAMS etching. In this work, we introduce a chemical scissor-mediated intercalation chemistry for structural editing of nonvdW MAX phases and vdW MXenes. The range of constituent elements of MAX phases and terminating groups of MXenes is greatly extended. Structural editing by alternating LAMS and metal scissors leads to the exfoliation of MAX phases and MXenes into stacked lamellae directly in molten salts and guides the discovery of a series of 2D metal-intercalated layered carbides.

Chemical scissor-mediated structural editing routes

The chemical scissor-mediated structural editing protocol contains four reaction routes



The periodic table emphasizes elements that are represented in MAX phases and MXenes (Fig. 1B). Aside from usual main-group elements (such as Al, Ga, and Sn), unconventional elements (Bi, Sb, Fe, Co, Ni, Cu, Zn, Pt, Au, Pd, Ag, Cd, and Rh) were intercalated into MAX phases. Meanwhile, in addition to the known halogen (-Cl, -Br, and -I) and chalcogen (-S, -Se, and -Te) terminations, the -P and -Sb (group 15 elements) terminations are demonstrated. All reaction recipes used in this study are listed in table SI.

Topotactic structural transformation of MAX phases aided by LAMS scissors

The Cu²⁺ cation in a LAMS scissor CuCl₂ has a strong electron affinity and can oxidize Al atoms that are weakly bonded in MAX phases (route I), as shown in Eqs. 1 and 2. As soon as interlayer atom vacancies $V_{\rm A}$ (denoted by \Box in $M_{n+1} \square X_n$) are available, predissolved guest metal atoms A' (e.g., Ga, In, or Sn) in molten salt diffuse into interlayers and occupy V_A to form $M_{n+1}A'X_n$ phases (Eq. 3) in a topotactic structural transformation manner (route II) (figs. S1 to S5). The A-element etching (vacancy formation) and intercalation (guest atom occupancy) are transient and concerted processes. The inserted guest atoms keep the interlayer space accessible to intercalants and prevent the etched $\mathbf{M}_{n+1}\square \mathbf{X}_n$ from collapsing into a close-packed, twin-like structure. Notably, the LAMS scissor should preferentially etch the A atoms in MAX phases but avoid the oxidation of intercalating metals (fig. S6) (22). Because of the thermodynamically favorable occupation of $V_{\rm A}$ vacancies, main-group metals with low melting points (T_m) diffuse into $M_{n+1} \square X_n$ to form stable MAX phases. Accordingly, with the aid of LAMS CdCl₂, Sb ($T_{\rm m}$ = 613°C) was successfully intercalated into a series of MAX phases such as Ti₃SbC₂, Ti₃SbCN, Nb₂SbC, and $Ti_3(Sb_{0.5}Sn_{0.5})CN$ (figs. S7 to S9). In the x-ray diffraction (XRD) pattern of Ti₃SbC₂, the (000l) peaks shifted toward higher Bragg angles compared with the Ti₃AlC₂ precursor (Fig. 2A), which indicates a shrinkage of lattice parameter c from 18.578 Å for Ti₃AlC₂ to 18.443 Å for Ti₃SbC₂ (fig. S10 and table S2). A similar decrease of lattice parameter c, but increase of a, was also observed in Nb₂SbC

2024

(a=3.329 Å and c=13.210 Å) as compared with Nb₂AlC (a=3.107 Å and c=13.888 Å). The strong coupling between the Sb 4p orbital with Ti 3d and Nb 4d orbitals accounts for the shortened bonding length along the c axis (23). Scanning transmission electron microscopy (STEM) imaging of Ti₃SbC₂ showed a typical zigzag pattern of the MAX phase along the $[11\bar{2}0]$ zone axis (Fig. 2B). Lattice-resolved STEM combined with energy dispersive spectroscopy (EDS) and scanning electron microscopy (SEM) further corroborated the absence of Al in final Ti₃SbC₂, which indicates the complete substitution of Al by Sb through the LAMS scissor-mediated intercalation (fig. S11):

$$3Cu^{2+} + 2Al = 3Cu + 2Al^{3+}$$
 (1)

$$M_{n+1}AIX_n = M_{n+1}\Box X_n + AI^{3+} + 3e^-$$
 (2)

$$\mathbf{M}_{n+1} \Box \mathbf{X}_n + \mathbf{A}' = \mathbf{M}_{n+1} \mathbf{A}' \mathbf{X}_n \tag{3}$$

Noble metals are seldomly considered as constituent elements of MAX phases because of their chemical inertness and high melting points (24). However, low eutectic points (EPs) of noble metals alloys, such as Au-Cd (EP ≈ 629°C), Ag-Sb (EP ≈ 484 °C), Pd-Sn (EP ≈ 600 °C), Pt-Cd (EP ≈ 670 °C), and Rh-Sn (EP ≈ 660 °C) can promote the noble metal intercalation into the interlayer atom vacancy of $M_{n+1} \square X_n$ etched by LAMS scissor CdCl2, and lead to the formation of noble metal-containing MAX phases: Nb₂AuC (Fig. 2, C and D, and fig. S12), Nb₂(Au_{0.5}Al_{0.5})C (fig. S13), Nb₂(Ag_{0.3}Sb_{0.4}Al_{0.3})C (fig. S14), $Nb_2(Pd_{0.5}Sn_{0.5})C$ (Fig. 2, E and F, and fig. S15), Nb₂PtC (fig. S16), Nb₂(Pt_{0.6}Al_{0.4})C (fig. S17), and Nb₂(Rh_{0.2}Sn_{0.4}Al_{0.4})C (fig. S18). Late transition metals in the fourth period (Fe, Co, Ni, Cu, and Zn) can also fully substitute for Al in Nb₂AlC aided by the same scissor, CdCl₂, and produce Nb₂FeC, Nb₂CoC, Nb₂NiC, Nb₂CuC, and Nb₂ZnC (Fig. 2, G and H, and figs. S19 to S24). The formation of MAX phases with transition metals in the A layer implicates the possibility of tuning their interlayer non-vdW bonding by orbital interaction of d-block electrons. However, the elements in groups 11 and 12 have saturated d orbitals, and their coupling with the d orbital of the transition metal becomes weak (23), which results in a small difference between the lattice parameters of Nb₂AuC (a = 3.175 Å and c =14.062 Å) and Nb₂AlC (a = 3.107 Å and c =13.888 Å), although the atomic radius of Au (146 pm) is much larger than that of Al (121 pm). The successful incorporation of noble metals with large atomic radii reflects the excellent structural tolerance and agile composition tunability in layered transition metal carbides.

In addition to monoatomic substitution, a double layer of Bi atoms in a MAX-like phase Nb_2Bi_2C was observed (Fig. 2I and fig. S25) in analogy with the well-studied Mo_2Ga_2C (25).

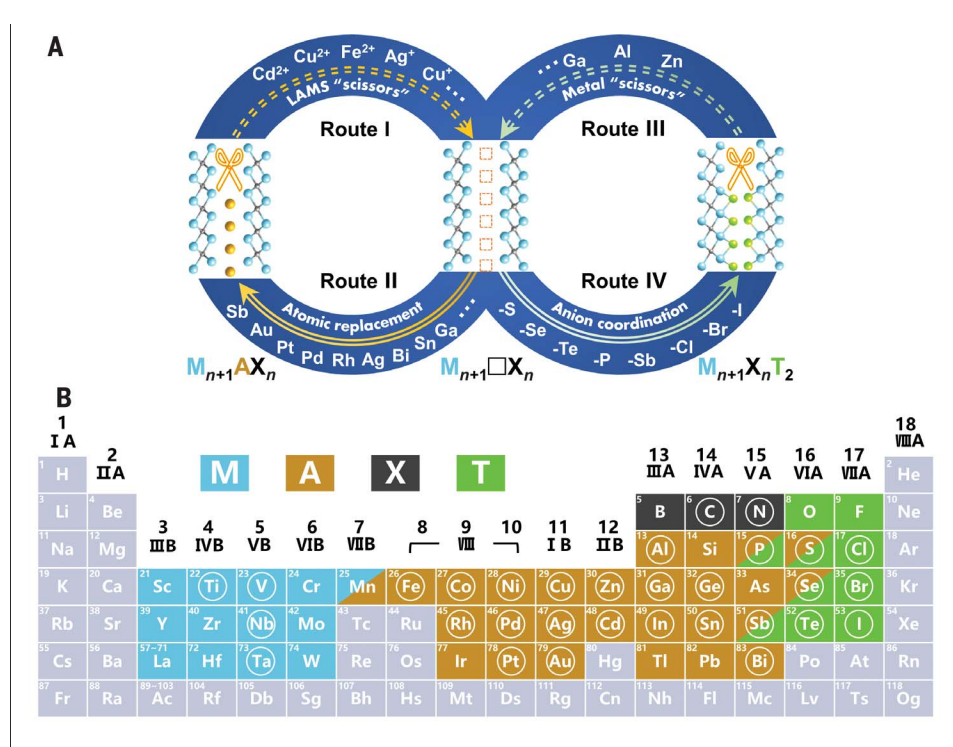


Fig. 1. Structural editing protocol of MAX and MXene mediated by the chemical scissors. (A) Schematic illustration of structural editing of MAX phases and MXenes through chemical scissor–mediated intercalation protocol. $M_{n+1}\square X_n$ denotes the structure with interlayer atom vacancies that formed after A-element etching. (B) Periodic table showing elements involved in the formation of MAX phases and MXenes. Light blue, M elements; brown, A elements; black, X elements; green, ligand (T) elements; circled, elements studied in the present work.

This means that the chemical scissor–mediated protocol can not only enrich the elemental composition but can also expand the structural diversity of layered carbides.

Diverse surface terminations of MXenes guided by the hard and soft acid and base principle

After the redox-driven etching of A element, further oxidation of $M_{n+1} \square X_n$ by LAMS scissors (Eq. 4) results in the formation of 2D MXenes (route IV). This means that high oxidationstate M atoms in $M_{n+1} \square X_n$ could accept the nonbonding electron pair from Lewis base T- (e.g., Cl-, Br- and I-) in molten salts and form planar coordination structures (Eq. 5). Moreover, the stability of these coordination structures of MXenes is largely determined by the hard and soft acid and base (HSAB) principle when several Lewis bases coexist in a molten salt. Most of the transition metal cations (such as Ti⁴⁺, Zr⁴⁺, and V⁵⁺) with high positive charges are typical hard Lewis acids (26). Consequently, the increase in chemical hardness of the halogen ligands (i.e., -I < -Br < -Cl < -F) strengthens the stability of resultant adducts, which explains the prevailing F-terminated MXenes obtained through various HF etching protocols (10). Although S²

anion is a soft base, it could be more energetically favorable to coordinate with transition metals than Cl^- , which is consistent with the fact that the O^{2-} terminal is more stable than F^- in HF-etched MXenes. Indeed, when S^{2-} was fed by ionic compounds, FeS or CuS, into chloride melts, S-terminated MXene $\mathrm{Ti}_2\mathrm{CS}_x$ and $\mathrm{Ti}_3\mathrm{C}_2(\mathrm{S}_{0.5}\mathrm{Cl}_{0.5})_x$ were obtained (fig. S26):

$$M_{n+1} \Box X_n = M_{n+1} \Box X_n^{2+} + 2e^-$$
 (4)

$$M_{n+1}\Box X_n^{2+} + xT^- = M_{n+1}X_nT_x$$
 (5)

HSAB-guided coordination assists the formation of other chalcogenide MXenes (T = -Se and -Te) in molten chloride salts (figs. S27 to S31). For example, a LAMS scissor CuI etches Al out of Nb2AlC (Eq. 2) and simultaneously oxidizes Nb atoms to a higher oxidation state (Eq. 4). The produced Cu reacts with Te ($T_{\rm m} \approx 450 \, ^{\rm o}$ C) in the chloride melt to form the ionic Cu₂Te compound with the eutectic point of 610°C (figs. S32). Last, Te²⁻ anions released from Cu2Te and driven by electrostatic forces diffuse into positively charged Nb₂□C interlayers to form coordination with Nb atoms (Eq. 5). An accordion-like morphology is shown in the SEM image of the resultant Nb₂CTe_x MXene (Fig. 3A). The appearance

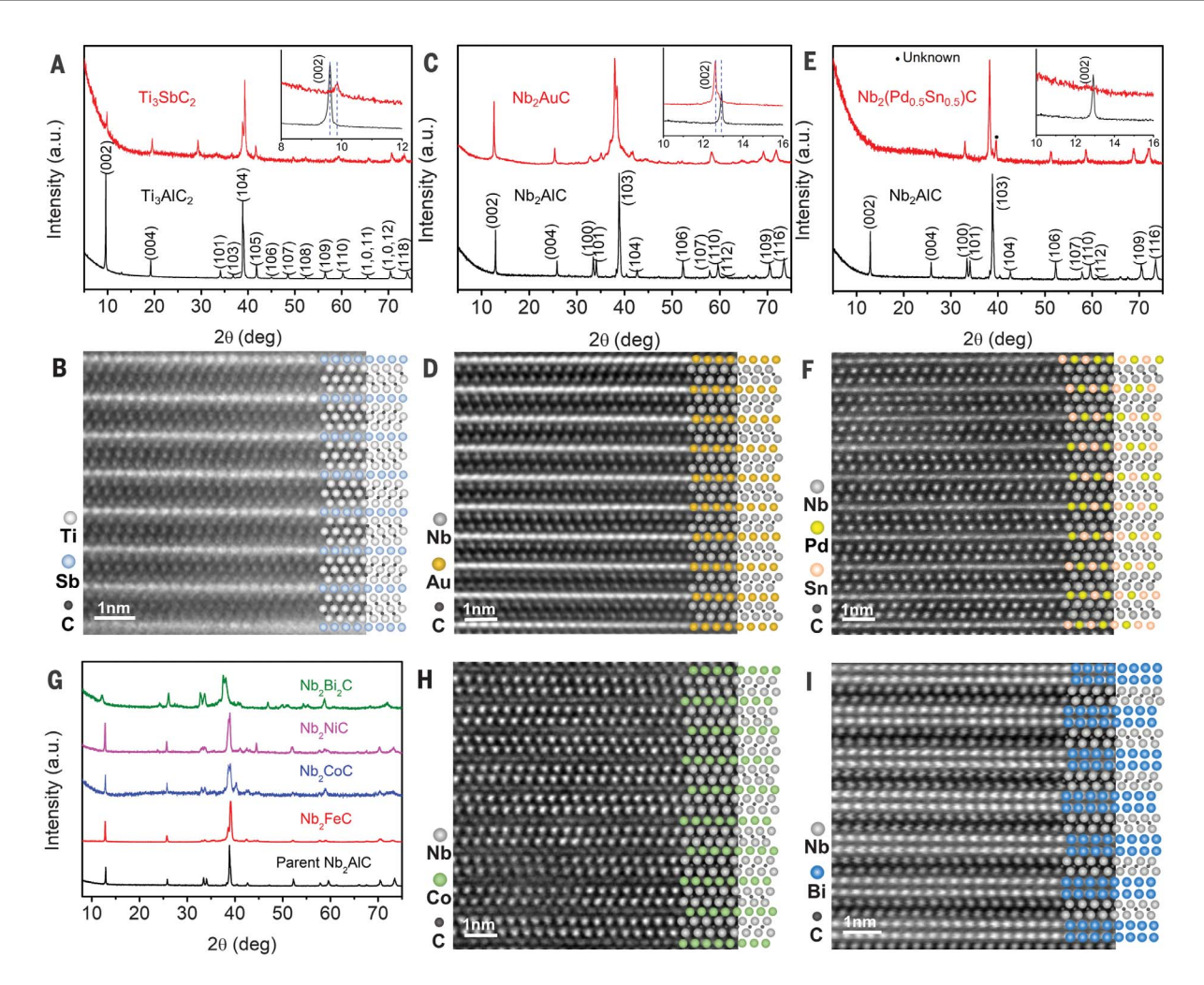


Fig. 2. Transformation of a MAX phase to another MAX phase. (A) XRD patterns of Ti_3SbC_2 and its parent phase Ti_3AlC_2 . (B) STEM image of Ti_3SbC_2 . (C) XRD patterns of Nb₂AuC and its parent phase Nb₂AlC. (D) STEM image of Nb₂AuC. (E) XRD patterns of Nb₂(Pd_{0.5}Sn_{0.5})C and its parent phase Nb₂AlC. (F) STEM image of Nb₂(Pd_{0.5}Sn_{0.5})C. (G) XRD

spectra of a series of MAX phases from Nb₂AlC: Nb₂FeC, Nb₂CoC, Nb₂NiC, and Nb₂Bi₂C. (**H** and **I**) STEM images of Nb₂CoC (H) and Nb₂Bi₂C (I). All STEM images were acquired along the $\left[11\bar{2}0\right]$ zone axis of MAX phases, and atomic structural models were added to corroborate the topotactic structural transition.

of (000*l*) peaks at low Bragg angles and the disappearance of MAX-phase diffraction peaks (Fig. 3B) confirmed the complete transformation from Nb₂AlC to Nb₂CTe_x. X-ray photoelectron spectroscopy (XPS) analysis further corroborates the coordination of Te with Nb ($E_{\rm Nb3d}$ = 203.5 and 206.3 eV) (Fig. 3, C and D, figs. S33 and S34, and table S3) (27).

To form atom vacancies $V_{\rm A}$ during etching in melts, chemical scissor CuI was added in the amount sufficient for removing Al out of Nb₂AlC. A closely packed, twin-like Nb₂C structure with a typical zigzag atom arrangement was observed (Fig. 3, E and F, and fig. S35), implicating the existence of interlayer atom vacancies between Nb₂C layers, which provide the space accessible for ligand coordination and atom intercalation. Both STEM-EDS and SEM-EDS analyses semi-quantitatively iden-

tified the termination stoichiometry of $x \approx 1$ in Nb₂CTe₂₂ which manifests a different coordination structure with a two-electron chalcogen (Te) that bridges Nb atoms when compared with the halogen-terminated MXenes ($x \approx 2$) (fig. S36) (13, 19, 21). A ripple-like atomic arrangement appeared in Nb₂CTe_x along the c plane (Fig. 3, G and H, and fig. S37). This should be attributed to the lattice stress caused by large Te atoms (ionic radius = 221 pm). Actually, the lattice parameters ($a \approx 3.403 \text{ Å}$ and $c\approx 20.130$ Å) of $\mathrm{Nb_2CTe}_x$ are significantly larger than those of the parent MAX phase Nb₂AlC ($a \approx 3.106 \text{ Å}$ and $c \approx 13.888 \text{ Å}$) (fig. S38 and table S2) (28). The enlarged a value (~9.5% increase) indicates a substantial in-plane tensile stress exerted by Te on the Nb₂C layers. Indeed, the ripple-like morphology almost disappears in MXene Ta₂CSe_x (Fig. 3, I and J, and fig. S39) because Se has a smaller ionic radius of 198 pm. Furthermore, a series of mixed terminations of chalcogen and halogen, such as $T = Te_{1-x}Cl_x$, $Te_{1-x}Br_x$, and $Te_{1-x}I_x$ (x = 0 to 1), could be arbitrarily tuned by controlling the molar ratios of elements in their precursors (figs. S40 to S42).

The proposed approach can be used to expand the range of possible surface terminations. For example, phosphorus is a volatile and reactive element that cannot be directly used to functionalize MXenes. We observed that as soon as the $\rm Ti_3AlC_2$ was etched by LAMS scissor $\rm CuBr_2$, $\rm P^{3^-}$ anions released from an ionic compound $\rm Cd_3P_2$ (EP $\approx 740^{\circ}\rm C)$ easily attacked $\rm Ti_3C_2$ together with $\rm Br^-$ to form a $\rm Ti_3C_2(P_{0.4}\rm Br_{0.6})_x$ MXene (figs. S43 and S44). Following the same exfoliation mechanism, we obtained two Sb-terminated MXenes, $\rm Ta_2CSb_x$ and $\rm Ta_4C_3Sb_x$ (figs. S45 to S47). We also observed a ripple-like morphology in

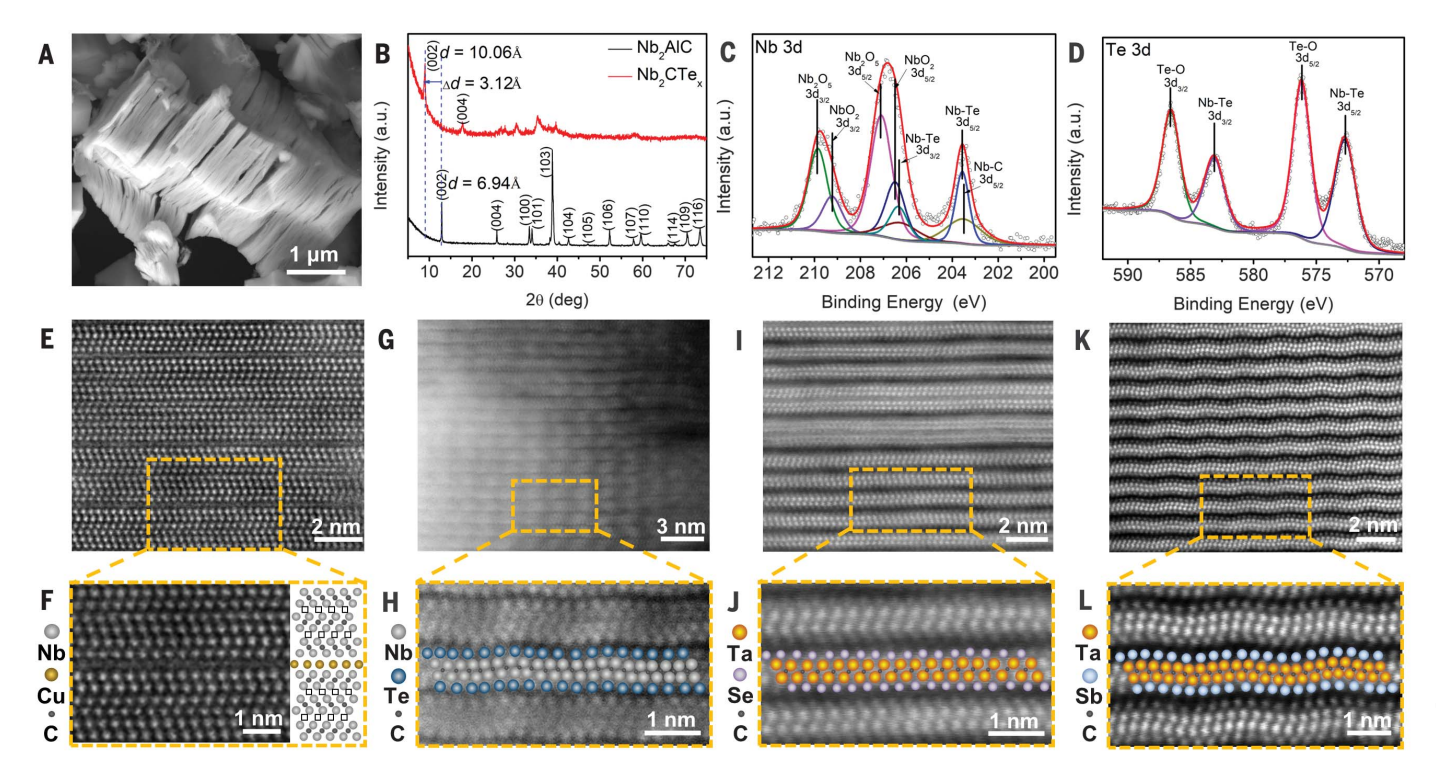


Fig. 3. Conversion from MAX phase to MXene. (**A**) SEM image of Nb₂CTe_x. (**B**) XRD patterns of Nb₂AlC and derived Nb₂CTe_x. Δd represents the swelling of interlayer spacing after chemical etching. (**C** and **D**) Nb 3d orbital (C) and Te 3d orbital (D) XPS spectra of Nb₂CTe_x. (**E**) STEM image revealing a close-packed, twin-like structure of Nb₂C and (**F**) the typical zigzag structure

with interstitial voids denoted by black boxes in the structure, implicating the formation of interlayer atom vacancies after etched-out Al atoms. (**G**) STEM image of Nb₂CTe_x along the [$11\bar{2}0$] zone axis and (**H**) their ripple-like morphology. (**I** and **J**) STEM images of Ta₂CSe_x. (**K** and **L**) STEM images of Ta₂CSb_x showing the similar ripple-like morphology.

 Ta_2CSb_x because the atomic radius of Sb is similar to that of Te (Fig. 3, K and L).

Reconstruction of 3D MAX phases from 2D MXenes enabled by metal scissors

This chemical scissor-mediated intercalation protocol is also applicable to editing MXenes. The Lewis basic ligands on MXenes can be removed by chemical scissoring of reductive metals (M') with a low electron affinity. From the point of view of coordination, the electrons donated by reductive metals refill the unoccupied d orbitals of transition metal cations in MXenes (reduction reaction), reducing the effective coordination centers for the ligands, which share their electron pairs. Therefore, M atoms in $M_{n+1} \square X_n$ are reduced to a lower oxidation state, and terminations are removed from MXenes (Eq. 6) (route III). The regained nonterminated $M_{n+1} \square X_n$ provides 2D building blocks for 3D MAX phase reconstruction when guest atoms reoccupy the interlayer vacancies (Eq. 7) (route II). Taking the well-studied Ti₃C₂Cl₂ MXene as an example, the metal scissor Ga removed -Cl terminations to form nonterminated $Ti_3\Box C_2$ (fig. S48). The evaporation of gaseous $GaCl_3$ ($T_b \approx 201$ °C) helps the complete removal of chlorine. The intercalation of guest atoms (Ga, Al, and Sn) stitched resultant $Ti_3\Box C_2$ layers to reconstruct the MAX phases $(Ti_3\Box C_2, Ti_3AlC_2, and Ti_3SnC_2)$, which was confirmed by XRD patterns (Fig. 4A). Atomically resolved STEM images (Fig. 4, B to F) verify the phase conversion from $Ti_3C_2Cl_2$ MXene via nonterminated $Ti_3\Box C_2$ to final reconstructed MAX phases:

$$M_{n+1}X_nT_x + M' = M_{n+1}\Box X_n + M'T_x$$
 (6)

$$M_{n+1} \square X_n + A' = M_{n+1} A' X_n$$
 (7)

We observed wide gaps in nonterminated Ti₃□C₂ when Cl terminations were removed from Ti₃C₂Cl₂ (Fig. 4C). EDS analysis confirmed the presence of Ga atoms distributed in the gaps, which kept the nonterminated $Ti_3 \square C_2$ from collapsing into close-packed, twin-like phase (fig. S48). The gap spacing seemed large enough to accommodate more than one layer of atoms. Indeed, Ti₃Cd₂C₂ with a double layer of Cd (Fig. 4G) was reconstructed when metal scissor Al and intercalant metal Cd were used. Most reconstructed MAX-phase particles preserve the accordionlike morphology of multilayer MXenes (fig. S49), which indicates that the removal of terminals by metal scissors and subsequent guest atom intercalation only happens between adjacent MXene lamellas separated by no more than vdW distance.

Multiple interconversions between MAX phases and 2D MXenes could further enrich the structural editing of layered carbides. First, Ti₃AlC₂ was exfoliated by chemical scissor CdCl₂ to form Ti₃C₂Cl₂ MXene (routes I and IV). Then, the synthesized multilayer Ti₃C₂Cl₂ MXene was reconstructed by chemical scissor Al back into multilayer Ti₃AlC₂ (routes III and II). The characteristic (0002) diffraction peaks of Ti₃C₂Cl₂ and Ti₃AlC₂ confirm the successful interconversion by means of LAMS etching and metal-aided reconstruction and become substantially broadened after three cycles of interconversion because of the reduced layer thickness (Fig. 4H). The fully exfoliated Ti₃AlC₂ and Ti₃C₂Cl₂ lamellae were finally formed (Fig. 4, I to L, and fig. S50). The spacing between these lamellae is sufficiently large for ions to access, which may benefit diffusion-controlled electrochemical and catalytic applications. When Sn was used as an intercalant in the final reconstruction step, Ti₃SnC₂ nanosheets were built up from Ti₃C₂Cl₂ nanosheets (Fig. 4M). STEM images revealed that Ti₃SnC₂ nanosheets belong to a family of metal-intercalated 2D carbides in which adjacent Ti₃C₂ lamellae are intercalated by monolayers of Sn atoms but have -Cl

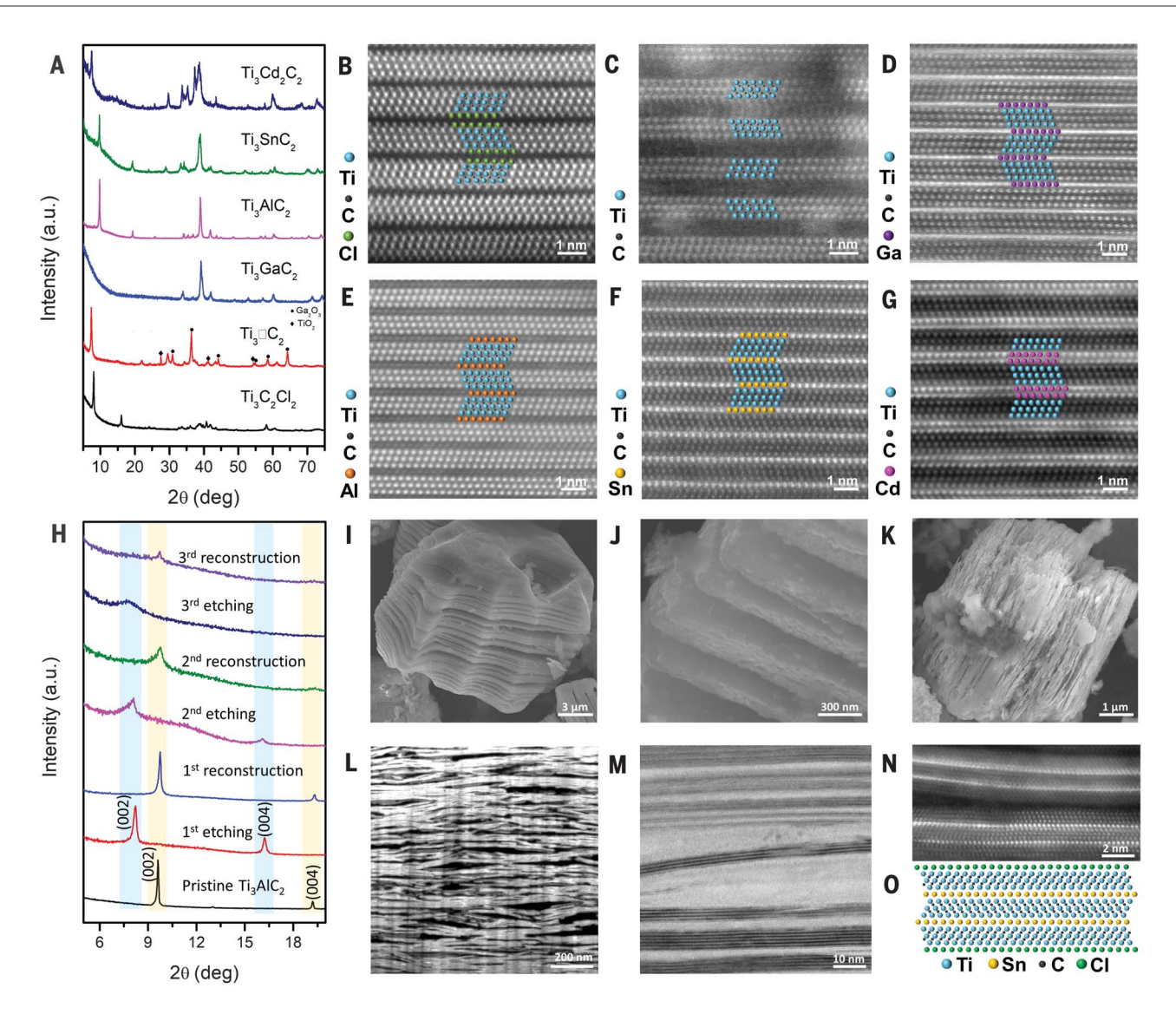


Fig. 4. Reconstruction of MAX phases from MXenes. (**A**) XRD patterns of the conversion of $Ti_3C_2Cl_2$ MXene to different MAX phases. (**B** to **G**) STEM image of $Ti_3C_2Cl_2$ MXene (B), Ga-filled $Ti_3\Box C_2$ after removal of terminals (C), Ti_3GaC_2 (D), Ti_3AlC_2 (E), Ti_3SnC_2 (F), and $Ti_3Cd_2C_2$ (G) along the $\begin{bmatrix} 11\bar{2}0 \end{bmatrix}$ zone axis. (**H**) XRD patterns showing the products after multiple etching and reconstruction. (**I** to **K**) SEM images of Ti_3AlC_2 obtained after one round (I), two rounds (J),

and three rounds (K) of etching and reconstruction, respectively. (**L**) The cross-section image of the product after three rounds of etching and reconstruction, showing the stacking structure of the Ti_3AlC_2 lamellae. (**M**) Bright-field STEM image of Sn-intercalated carbide lamellae at a low magnification. (**N** and **O**) Dark-field STEM image showing atomically resolved structure of Sn-intercalated carbide $Ti_9Sn_2C_6Cl_x$ (N) and its corresponding atomic structure (O).

terminations on the outmost surface (Fig. 4N and fig. S51). Therefore, such reconstructed metal-intercalated carbides combine both the functional features of MXenes that have tunable surface terminations and the structural features of MAX phases that possess oxidation-resistant interlayers. Metal-intercalated 2D carbides with the formula $M_{(n+1)m}A_{m-1}X_{nm}T_x$ (A, intercalated atom; m, number of layers) can be defined if m layers of stacked MXenes $M_{n+1}X_nT_x$ are intercalated by (m-1) layers of guest atoms after removal of (m-1) interlayer terminals by metal scissors (Eqs. 8 and 9). A Snintercalated 2D carbide $T_{ig}Sn_2C_6Cl_x$ is obtained where n=2 and m=3 (Fig. 4O). If m=1, then

there is no intercalation at all, and the atom-intercalated 2D carbide has the same formula as MXene $\mathbf{M}_{n+1}\mathbf{X}_n\mathbf{T}_x$. If m is large enough, surface terminations can be neglected for thick lamellae and the formula $\mathbf{M}_{(n+1)m}\mathbf{A}_{m-1}\mathbf{X}_{nm}\mathbf{T}_x$ is reduced to $\mathbf{M}_{n+1}\mathbf{A}\mathbf{X}_n$, which represents the bottom-up reconstruction of 2D MXene nanosheets into 3D MAX phase particles:

$$mM_{n+1}X_nT_x + (m-1)M' = M_{(n+1)m} \square_{m-1}X_{nm}T_x + (m-1)M'T_x$$
 (8)

Conclusions

The chemical scissor–mediated structural editing of MAX phases and their derived MXenes provides a powerful and versatile protocol to engineer the structure and composition of both vdW and non-vdW layered materials. The regulated intercalation routes allow the incorporation of unconventional elements into the monoatomic layer of MAX phases, which cannot be achieved through traditional metallurgic reactions, and enable the terminals' regulation of MXenes. Metal-intercalated 2D carbides, which combine the distinct structural features of MAX phases and MXenes, can be constructed through the removal of surface terminations

of MXenes by metal scissors and the subsequent accommodation of guest atoms between the MXene lamellae, thus further expanding the family of layered materials. Future efforts should focus on the delamination of these 2D and 3D layered carbides, as well as metal-intercalated 2D carbides, into single- and few-layer nanosheets, which are needed for fundamental property characterization and for taking full advantage of these new materials in energy storage, electronics, and other applications.

REFERENCES AND NOTES

- 1. J. Zhou et al., Adv. Mater. 33, e2004557 (2021).
- 2. J. Wan et al., Chem. Soc. Rev. 45, 6742-6765 (2016).
- 3 M S Whittingham Science 192 1126-1127 (1976)
- T. Oshima, D. Lu, O. Ishitani, K. Maeda, Angew. Chem. Int. Ed. 54, 2698–2702 (2015).
- 5. F. Xiong et al., Nano Lett. 15, 6777-6784 (2015)
- 6. M. Burrard-Lucas et al., Nat. Mater. 12, 15-19 (2013).
- 7. X. Zhao et al., Nature 581, 171-177 (2020).
- M. W. Barsoum, Prog. Solid State Chem. 28, 201–281 (2000).
- M. Sokol, V. Natu, S. Kota, M. W. Barsoum, Trends Chem. 1, 210–223 (2019).
- 10. M. Naguib et al., Adv. Mater. **23**, 4248–4253 (2011).
- M. Naguib, V. N. Mochalin, M. W. Barsoum, Y. Gogotsi, Adv. Mater. 26, 992–1005 (2014).
- A. VahidMohammadi, J. Rosen, Y. Gogotsi, Science 372, eabf1581 (2021).

- 13. M. Li et al., J. Am. Chem. Soc. 141, 4730-4737 (2019).
- M. Ghidiu, M. R. Lukatskaya, M. Q. Zhao, Y. Gogotsi, M. W. Barsoum. *Nature* 516, 78–81 (2014).
- 15. Y. Shao et al., Nat. Commun. 13, 3223 (2022)
- 16. F. Shahzad et al., Science 353, 1137-1140 (2016).
- 17. Y. Li et al., ACS Nano 13, 9198-9205 (2019).
- 18. H. M. Ding et al., Mater. Res. Lett. **7**, 510–516 (2019). 19. M. Li et al., ACS Nano **15**, 1077–1085 (2021).
- 20 Y Li et al. Nat. Mater 19, 894–899 (2020)
- 21. V. Kamysbayev et al., Science 369, 979-983 (2020).
- 22. A. Zavabeti et al., Science 358, 332-335 (2017).
- 23. X. H. Zha et al., Inorg. Chem. 61, 2129-2140 (2022).
- 24. H. Fashandi et al., Nat. Mater. 16, 814–818 (2017).
- 25. C. C. Lai et al., Acta Mater. 99, 157-164 (2015).
- 26. T.-L. Ho, Chem. Rev. 75, 1-20 (1975).
- 27. M. K. Bahl, J. Phys. Chem. Solids 36, 485-491 (1975).
- I. Salama, T. El-Raghy, M. W. Barsoum, J. Alloys Compd. 347, 271–278 (2002).

ACKNOWLEDGMENTS

We thank P.F. Yan and X.L. Mu (Beijing University of Technology) for STEM data and the corresponding analysis. Funding: This work was supported by Key R&D Projects of Zhejiang Province 2022C01236 (to Q.H., K.C., and K.L.); Leading Innovative and Entrepreneur Team Introduction Program of Zhejiang 2019R01003 (to Z.C. and O.H.): International Partnership Program of Chinese Academy of Sciences 174433KYSB20190019 (to Q.H.); Advanced Energy Science and Technology Guangdong Laboratory HND20TDTHGC00 (to Q.H); Ningbo Top-talent Team Program and Ningbo "3315 plan" 2018A-03-A (to Z.C.); National Natural Science Foundation of China (21671195, 52172254, 52250005, 52202325, and U2004212) (to Q.H., S.D., M.L., and Y.L.); China Postdoctoral Science Foundation 2020M680082 (to Y.L.): Knut and Alice Wallenberg Foundation through the Wallenberg Academy Fellows Program KAW 2020.0196 (to P.E.) and the Wallenberg Scholar Program KAW 2019.0290 (to L.H.); the

Swedish National Infrastructure in Advanced Electron Microscopy (2021-00171 and RIF21-0026) (to P.O.Å.P.); Swedish Government Strategic Research Area in Materials Science on Functional Materials at Linköping University SFO-Mat-LiU 2009 00971 (to P.O.Å.P., P.E., and L.H.); and US National Science Foundation DMR-2041050 (to Y.G.). Author contributions: Q.H. initiated and supervised the experimental work; Y.G. directed the discussion; H.D. conducted main experiment and analyzed results with Y.L. and MI: II IP POAP and GC conducted the TFM analysis and interpretation with contributions from L.H. and P.E.: H.D. and Q.H. wrote the manuscript with contributions from all coauthors; and all authors reviewed and commented on successive drafts of the manuscript. Competing interests: Q.H. and H.D. are inventors on patent applications (CN202111489021.0, CN202111330269.2, CN202111488622.X, CN202111488980.0) submitted by Ningbo Institute of Materials Technology and Engineering that cover the MAX phases and MXenes described in this paper. Y.G. is also affiliated with Sumy State University, Ukraine. Data and materials availability: All data are available in the manuscript or the supplementary material. License information: Copyright © 2023 the authors, some rights reserved; exclusive licensee American Association for the Advancement of Science. No claim to original US government works. https://www.science.org/about/sciencelicenses-journal-article-reuse

SUPPLEMENTARY MATERIALS

science.org/doi/10.1126/science.add5901 Materials and Methods Supplementary Text Figs. S1 to S51 Tables S1 to S3 References (29-46)

Submitted 28 July 2022; accepted 16 February 2023 10.1126/science.add5901